Journal of Alloys and Compounds 651 (2015) 405–413

Contents lists available at ScienceDirect

Journal of Alloys and Compounds

journal homepage: http://www.elsevier.com/locate/jalcom

Magnetic and transport properties assisted by local distortions in $Bi_2Mn_4O_{10}$ and $Bi_2Fe_4O_9$ multiferroic compounds

F.E.N. Ramirez [a], G.A. Cabrera-Pasca [a], J. Mestnik-Filho [b], A.W. Carbonari [b], J.A. Souza [a, *]

[a] Universidade Federal do ABC, Santo André 09210-580, SP, Brazil
[b] Instituto de Pesquisas Energéticas e Nucleares, Universidade de São Paulo, 05508-000 São Paulo, Brazil

ARTICLE INFO

Article history:
Received 18 June 2015
Received in revised form
19 August 2015
Accepted 20 August 2015
Available online 21 August 2015

Keywords:
Multiferroic
Magnetism
Electrical properties
Nuclear spectroscopy

ABSTRACT

We have performed a comprehensive study on the magnetic and electrical properties through macroscopic and local characterizations on $Bi_2Mn_4O_{10}$ and $Bi_2Fe_4O_9$. An analysis of the temperature evolution of local distortions, which was obtained by perturbed angular correlation measurements, revealed an anomalous behavior of the quadrupolar frequency and asymmetry parameter below the antiferromagnetic ordering temperature for both samples. The combined results suggest correlations between magnetic, electric, and elastic interactions. At high temperature, we have observed that the hopping frequency and activation energy in the electrical transport mechanism are close related to hyperfine parameters, electrical field gradient and asymmetry parameter, due to modifications in the equilibrium positions of oxygen atoms conforming octahedral, pyramidal, and tetrahedral environments. Anharmonic lattice effects are much more pronounced in a temperature range close to room temperature.

1. Introduction

Bismuth-based oxides with perovskite structure have been extensively studied for decades because they show ferroelectric and magnetic ordering simultaneously [1–3]. The coexistence of ferroelectric and magnetic order opens the possibility of controlling the electric polarization by application of a magnetic field or, contrarily, the magnetization with an applied electric field [4,5]. These electric and magnetic properties, therefore, make these compounds potential candidates for sophisticated devices and application in spintronic [6–9].

The $Bi_2Fe_4O_9$ and $Bi_2Mn_4O_{10}$ compounds are among the most interesting bismuth-based oxides with multiferroic properties. Both compounds exhibit a complex mullite-like crystal structure with space group *Pbam*. In $Bi_2Mn_4O_{10}$ compound, it has been observed that the Mn ions have mixed valence of (Mn^{3+} and Mn^{4+}) where Mn^{4+} ion is surrounded by six oxygen atoms forming an octahedron (Mn^{4+}–O_6) while the Mn^{3+} ion is surrounded by five oxygen atoms forming a tetragonal pyramid (Mn^{3+}–O_5) [10]. Distinctively, in the $Bi_2Fe_4O_9$ compound, the magnetic ion shows a single valence (Fe^{3+}) and is localized in two nonequivalent crystallographic sites with octahedral (Fe^{3+}–O_6) and tetrahedral (Fe^{+3}–O_4) coordination [11].

Both $Bi_2Mn_4O_{10}$ and $Bi_2Fe_4O_9$ belong to the type-II ferroelectric group, where the ordering of the electric dipolar moment exists only in the ordered magnetic phase. The magnetic phase transition from paramagnetic to antiferromagnetic state is found at Neel temperature of $T_N = 39$ K and 290 K for $Bi_2Mn_4O_{10}$ and $Bi_2Fe_4O_9$, respectively. Several works have shown that the Neel temperature is lower than the Weiss temperature (θ_W) in both compounds - for $Bi_2Mn_4O_{10}$ $|\theta_W| \approx 9T_N$ while for $Bi_2Fe_4O_9$ $|\theta_W| \approx 7T_N$ [12,13]. This effect reveals the presence of magnetic frustration between exchange interactions which is caused by the complex crystalline structure of these compounds. The magnetic frustration is minimized by magnetostriction effect in order to reach a long-range antiferromagnetic order. Experimentally, the degree of frustration of the magnetic structure can be quantified by using the index $f = |\theta_W|/T_N$ [14]. The ferroelectric ordering is driven by the magnetostriction effect which reduces the crystal structure symmetry [15]. The ferroelectric ordering takes place close to the antiferromagnetic transition leading to strong linear magnetoelectric coupling.

Despite the intense effort to understand the coupling mechanism between the electrical and magnetic properties, a better knowledge can be obtained when local distortions are correlated to macroscopic measurements. In order to address the temperature

* Corresponding author.
E-mail address: joseantonio.souza@ufabc.edu.br (J.A. Souza).

http://dx.doi.org/10.1016/j.jallcom.2015.08.165
0925-8388/

evolution of magnetic order and electrical transport at low and high temperature, we have performed a detailed local distortion study in $Bi_2Mn_4O_{10}$ and $Bi_2Fe_4O_9$ mullite-type compounds. Through the temperature dependence of the electrical-field gradient (EFG) and the asymmetry parameter (η), we were able to observe that local distortions are closely related to the appearance of magnetic and electric orders below T_N. Interesting, local structural evolution was also observed at high temperatures. The onset of these structural instabilities along with its correlation to the electrical transport macroscopic behavior is discussed.

2. Experimental details

$Bi_2Mn_4O_{10}$ and $Bi_2Fe_4O_9$ bulk samples were prepared by solid state reaction method by using metal oxides Bi_2O_3 (99.99%), Fe_2O_3 (99.99%), and MnO_2 (99.99%) as starting materials. Stoichiometry amounts of the metal oxides were mixed and intimately ground in an agate mortar. The resulting powder was carried to various heat treatments, being macerated between one and another, for 24 h. The temperature used in each heat treatment was 800, 850 e 900 °C (for $Bi_2Mn_4O_{10}$) and 700, 750 e 800 °C (for $Bi_2Fe_4O_9$), respectively. Finally, the powder samples were pressed into pellets and sintered in air atmosphere at 900 °C (for $Bi_2Mn_4O_{10}$) e 800 °C (for $Bi_2Fe_4O_9$) for 15 h, respectively. X-ray powder diffraction (XRD) experiments were performed on a $\theta-2\theta$ Bruker AXS D8 Focus diffractometer with Cu–Kα radiation. Structural parameters of both compounds were refined by using Rietveld method.

The macroscopic behavior of the physical properties was studied by magnetic and dc electrical resistivity measurements. Magnetic measurements were carried out in a "Physical Property Measurement System" (PPMS) from Quantum Design. DC electrical resistivity was measured in air by using a four-probe method by using a custom-built dedicated apparatus. Silver epoxy was used to connect the sample with the station which is composed of alumina and the wiring is made of platinum.

The local behavior of the physical properties was studied by Mössbauer spectroscopy and perturbed angular correlation (PAC) technique. ^{57}Fe Mössbauer spectra were recorded at room temperature by using a conventional spectrometer in sinusoidal mode and with a ^{57}Co/Rh γ-ray source. The source velocity was calibrated with pure iron metal at 300 K as a control material. Spectra were fitted with the NORMOS program [16]. PAC measurements were recorded with a spectrometer which consists of four BaF_2 detectors horizontally arranged and forming a cross configuration. ^{111}In(^{111}Cd) was used as probe nuclei which were introduced in small amounts (the ^{111}In final concentration was below 1 ppb) into samples by thermal diffusion method. The samples were put into alumina crucibles and sealed in a quartz tube under low pressure helium. Finally, the samples were heated to 800 °C for 20 h followed by fast cooling to room temperature. This heat treatment induces the thermal diffusion of the probe nuclei into the sample. PAC spectra were obtained in a wide temperature range (10 K < T < 700 K). In order to identify the crystallographic site where probe nuclei are localized, we have also performed first-principles calculations based on the density functional theory (DFT). These calculations simulate the introduction of Cd radioactive atoms in crystallographic sites that exist in our samples. The simulations were performed by means of the WIEN2k package which is an implementation of DFT with APW + LO basis functions [17]. In these calculations, a cationic site is substituted by one Cd atom at a time within the unitary cell. The relatively large concentration of atoms Cd at the sub-cell, where one cation was substituted by Cd, is a consequence of the existence of two atoms of Mn or Fe in the large unit cell that have the compound $Bi_2Mn_4O_{10}$ and $Bi_2Fe_4O_9$ (two unit formulas per each unit cell). On the other hand, the overall concentration of atoms Cd was only ~3% because there is 32 atoms within the unit cell. In WIEN2k, the cut-off energy of the base functions is determinated by the relation $R_{min}{}^{*}K_{max} = 7$, where R_{min} is the smallest of the muffin-tin radii and K_{max} is the largest reciprocal wave vector (for details, see Ref. [17]). The value of the cut-off energy was 260 eV. In order to describe the exchange and correlation potential, it was adopted the generalized gradient approximation (GGA) functional [18]. The integrations within the Brillouin zone were done with a modified tetrahedron method on a grid of 200 points [19].

3. Results and discussion

3.1. Macroscopic structural, magnetic, and electrical properties characterizations

Fig. 1(a) e (b) shows the X-ray diffraction pattern along with the Rietveld refinement obtained for the $Bi_2Mn_4O_{10}$ and $Bi_2Fe_4O_9$ compounds, respectively. Both samples are single-phase belonging to the orthorhombic space group *Pbam* – the Bragg reflections are very narrow reveling the bulk size of the grains. The unit cell parameters obtained from Rietveld refinements for $Bi_2Mn_4O_{10}$ are $a = 7.5572$ (1) Å, $b = 8.5299$ (1) Å, $c = 5.7585$ (1) Å, and $V = 371.21$ (1) Å^3 whereas for $Bi_2Fe_4O_9$ we have obtained $a = 7.9704$ (1) Å, $b = 8.4381$ (1) Å, $c = 6.0012$ (1) Å, and $V = 403.61$ (1) Å^3. Note that the unit cell volume of $Bi_2Fe_4O_9$ is larger than that for $Bi_2Mn_4O_{10}$. This result is due to the higher ionic radius of Fe^{3+} than that of Mn^{4+}. These values are in good agreement with data reported in the literature [20]. Fig. 1(c) shows the zero field cooling (ZFC) and field cooling (FC) measurements of the magnetic susceptibility as a function of temperature obtained with an applied magnetic field H = 1000 Oe for the two samples. The magnetic susceptibility of the two samples exhibits a maximum suggesting the appearance of long-range antiferromagnetic order (AFM). The Neel temperature, which was defined at this peak position, is 39 K and 250 K for $Bi_2Mn_4O_{10}$ and $Bi_2Fe_4O_9$, respectively. We have observed that the curve χ^{-1} vs T (not shown) of $Bi_2Mn_4O_{10}$ exhibits a linear behavior in the range temperature T > 100 K suggesting that the Curie–Weiss law is obeyed. This result indicates that the Mn magnetic ions do not interact with each other in the paramagnetic phase of this compound. For T < 100 K, the exchange magnetic interactions between the Mn ions are activated leading to the long-range magnetic order observed at 39 K. The values of the Weiss temperature (θ_W) and effective magnetic moment (μ_{eff}), obtained from the linear fitting by using the Curie–Weiss law, are $\theta_W = -260$ (3) K and $\mu_{eff} = 6.55$ (1) μ_B. The magnetic frustration index of this compound is $f = 6.67$ indicating a high degree of frustration between the exchange interactions. The value of μ_{eff} is very close to the expected value of 6.24 μ_B.

The electrical transport measurements (electrical resistivity (ρ)) as a function of temperature (300 K < T < 600 K) for $Bi_2Mn_4O_{10}$ and $Bi_2Fe_4O_9$ compounds are shown in Fig. 1(d). It is important to mention that these measurements were obtained by warming the sample to the highest temperature followed by cooling and repeated for at least three times. For the sample $Bi_2Mn_4O_{10}$, we have observed reproducibility of all measurements where the cooling and warming curves show a similar behavior. However, for the sample $Bi_2Fe_4O_9$, we have observed some anomalous behavior in the first measurement during the warming (not shown) which disappear during cooling and subsequent measurements. This anomalous behavior is due to adsorption/desorption of water vapor molecules on the sample surface. Fig. 1(d) shows the warming curve of the electrical resistivity obtained in the second measurement for $Bi_2Mn_4O_{10}$ and $Bi_2Fe_4O_9$ compounds. A thermally activated behavior, as would be expected from any wide bandgap

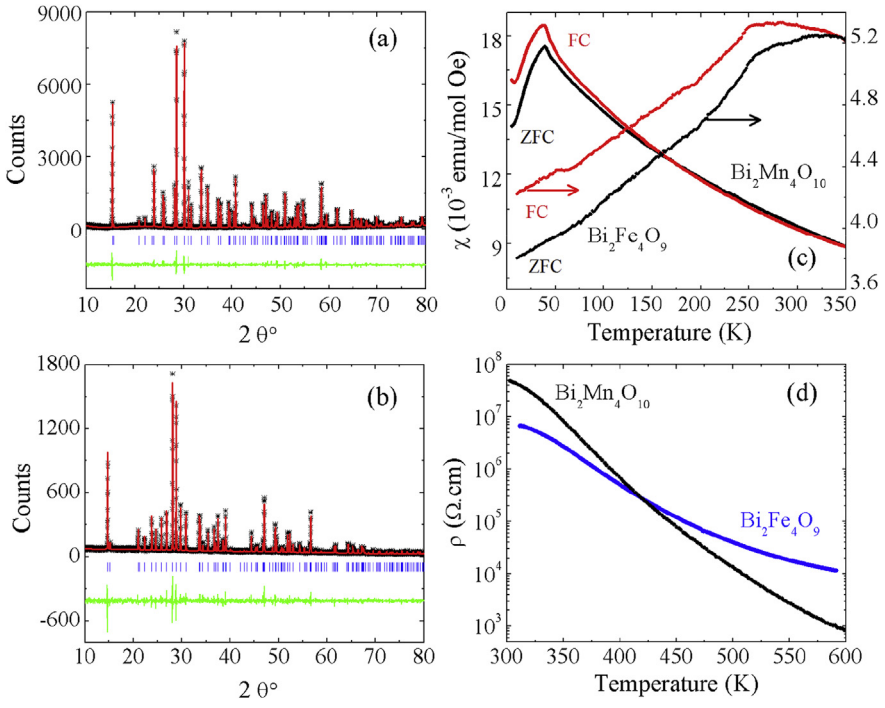

Fig. 1. X-ray powder diffraction pattern along with Rietveld refinement for (a) $Bi_2Mn_4O_{10}$ and (b) $Bi_2Fe_4O_9$. (c) Magnetization (ZFC and FC) as a function of temperature obtained with H = 1000 Oe for both compounds. (d) Temperature dependence of the dc electrical resistivity for $Bi_2Mn_4O_{10}$ and $Bi_2Fe_4O_9$ samples.

semiconductor, is clearly observed for both samples. Furthermore, we can see that the electrical resistivity magnitude decreases significantly with the temperature. For $Bi_2Mn_4O_{10}$ ($Bi_2Fe_4O_9$), it decreases almost five (three) order of magnitude. Note also that for 300 K < T < 425 K, the value of ρ is larger in $Bi_2Mn_4O_{10}$ whereas that for T > 425 K the sample $Bi_2Fe_4O_9$ has a larger value of ρ. The formation of impurity crystallographic phases in both samples was discarded by XRD experiments obtained after these electrical resistivity measurements at high temperature. Mainly due to the magnetic structure point of view, the mechanism that governs the transport properties is suggested to be different in each sample. The charge transport in $Bi_2Mn_4O_{10}$ takes place intrinsically by electronic hopping between mixed valence Mn^{3+} and Mn^{4+} ions. On the other hand, it is known that the presence of slight oxygen deficiency (oxygen vacancies) in $Bi_2Fe_4O_9$ may create Fe^{2+} ions within the iron sub-lattice. The coexistence of Fe^{2+} and Fe^{3+} on the surface of the

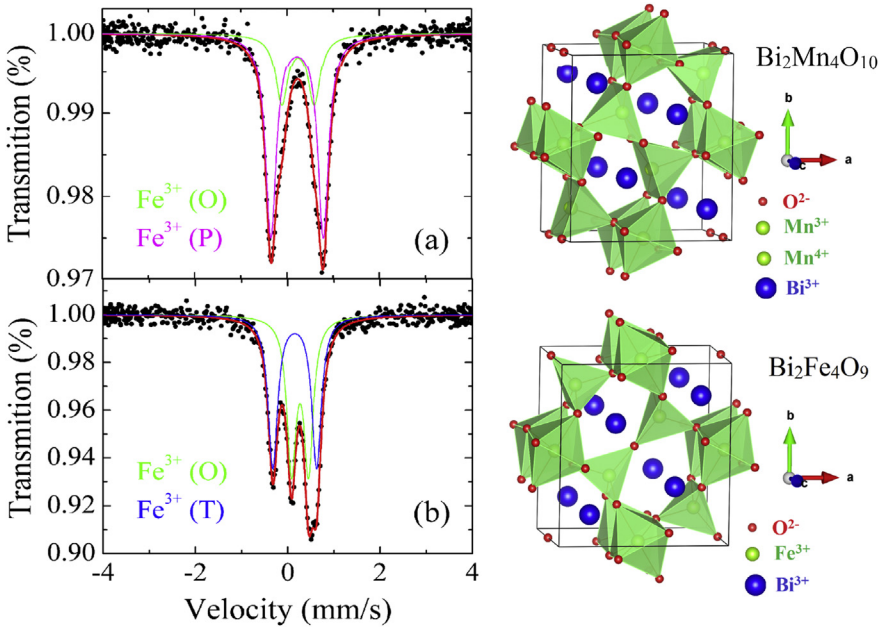

Fig. 2. (left) Mössbauer spectra obtained at room temperature for (a) $Bi_2Mn_4O_{10}$ doped with 25%Fe and (b) $Bi_2Fe_4O_9$, respectively. The solid lines correspond to the fit considering two crystallographic sites for the ion Fe^{3+}. O: octahedral, P: pyramidal, and T: tetrahedral. (right) The crystal unit cells of $Bi_2Mn_4O_{10}$ and $Bi_2Fe_4O_9$ compounds.

grains in the octahedral/tetrahedral sites favors the electron hopping conduction between Fe^{2+} and Fe^{3+} ions besides the intrinsic semiconducting contribution. Eventually, the oxygen vacancies delocalization may also be activated and contribute to the electrical conductivity of $Bi_2Fe_4O_9$ compound.

3.2. Local distortion characterization

In order to perform a comparative study about the temperature evolution of the local distortions with the macroscopic behavior observed in the magnetic and transport properties of our samples, we carried out Mössbauer spectroscopy and PAC measurements. Fig. 2 shows Mössbauer spectra of $Bi_2Mn_4O_{10}$ and $Bi_2Fe_4O_9$ obtained at room temperature. Small amount of Fe probes was introduced in $Bi_2Mn_4O_{10}$ which does not change the crystalline phase – XRD experiments revealed isostructural phase with respect to undoped $Bi_2Mn_4O_{10}$ compound. Only paramagnetic doublets produced by pure electronic quadrupolar interactions are present confirming the paramagnetic state at room temperature. The Mössbauer hyperfine parameters such as paramagnetic isomer shift (IS) and quadrupole splitting (QS) are obtained. Mössbauer spectra of $Bi_2Mn_4O_{10}$ and $Bi_2Fe_4O_9$ compounds are given by a superposition of two quadrupolar doublets due to Fe^{3+} of similar intensity where the sub-spectrum with the smaller quadrupolar splitting is attributed to octahedrally coordinated iron.

For both samples, an excellent fitting of Mössbauer spectra was achieved by using two paramagnetic doublets of Fe^{3+}. For the sample $Bi_2Mn_4O_{10}$, the values of the isomer shift and quadrupolar splitting obtained from the fitting are IS = 0.375 mm/s and QS = 0.382 mm/s (for the octahedral site) and IS = 0.262 mm/s and QS = 0.965 mm/s (for the pyramidal site). On the other hand, for the sample $Bi_2Fe_4O_9$, we have obtained IS = 0.357 mm/s and QS = 0.71 mm/s (for the octahedral site); and IS = 0.331 mm/s and QS = 1.12 mm/s (for the tetrahedral site). From the fitting, we can also obtain the adsorption area (A) which is proportional to the amount of iron localized at crystallographic site. For $Bi_2Mn_4O_{10}$, the values obtained are A = 28% and 72% for the octahedral and pyramidal sites, respectively. This result indicates that the Fe ions are distributed preferentially on the pyramidal site. Interesting, this result also reveals that in spite of the preferential occupation of the pyramidal site, there is a small amount of Fe^{3+} ion substituting to manganese ions with different valence (Mn^{4+}). For $Bi_2Fe_4O_9$, we have obtained A = 48% and 52% for the octahedral and tetrahedral sites, respectively. The crystal unit cells of these compounds are showed in the right side of Fig. 2. In this case, the Fe ions are distributed homogeneously in both crystallographic sites. Another important result is the absence of paramagnetic sites corresponding to Fe^{2+} ions in both samples. The absence of Fe^{2+} sites allows discard the presence of Fe_3O_4 as spurious phase which usually grows in the synthesis process of $Bi_2Fe_4O_9$.

The spin rotation spectrum measured by PAC spectroscopy is given by $R(t) = A_{22}\sum_i f_i G^i_{22}(t)$, where $G_{22}(t)$ is the perturbation function which describes the time modulation of the angular correlation perturbed by the hyperfine interaction and f_i are the fractional site populations of probe nuclei. For a static quadrupole interaction, the perturbation function has the form $G_{22}(t) = S_{20} + \sum_{n=1}^{3} S_{2n}\cos(\omega_n t)\exp(-\delta\omega_n t)$. The frequencies ω_n are related to the quadrupole frequency $\nu_Q = eQVzz/h$ by $\omega_n = g_n(\eta)\,\nu_Q$, where Q is the nuclear electric quadrupole moment of the intermediate level of nuclear probe, and the exponential factor accounts for a frequency distribution of width δ around ω_n. The coefficients $g_n(\eta)$ are known functions of the asymmetry parameter $\eta = (V_{xx} - V_{yy})/V_{zz}$, where V_{kk} (k = x,y,z) denotes the principal component of the electric field gradient (EFG) tensor. It provides information about the behavior of the local electric field gradient in the crystallographic site where the probe nuclei are localized. The parameter η, with values limited to $0 < \eta < 1$, measures the deviation of the local charge distribution from axial symmetry due to local distortion of the crystallographic site. For a pure dipole magnetic interaction, the Larmor frequency $\omega_L = \mu_N g B_{hf}/\hbar$ is directly determined from the PAC spectrum and, as long as the g-factor (g) of the probe nuclei is known, the magnetic hyperfine field B_{hf} is calculated. Representative curves of $R(t)$ spectra of PAC measurements taken above and below of the antiferromagnetic transition are showed in Fig. 3 for the compounds $Bi_2Mn_4O_{10}$ (T_N = 39 K) and $Bi_2Fe_4O_9$ (T_N = 260 K), respectively. Above T_N, we have achieved an excellent fitting of these spectra taking into account only electric quadrupolar interactions. Below T_N, the PAC spectra exhibit a clear attenuation for both samples which is caused simply due to the presence of combined interactions which broadens the hyperfine lines. Therefore, the PAC spectra were fitted take into account a combination of electric quadrupole and magnetic interactions. The hyperfine magnetic interactions are characterized by the Larmor frequency which is proportional to the magnetic hyperfine field (B_{hf}).

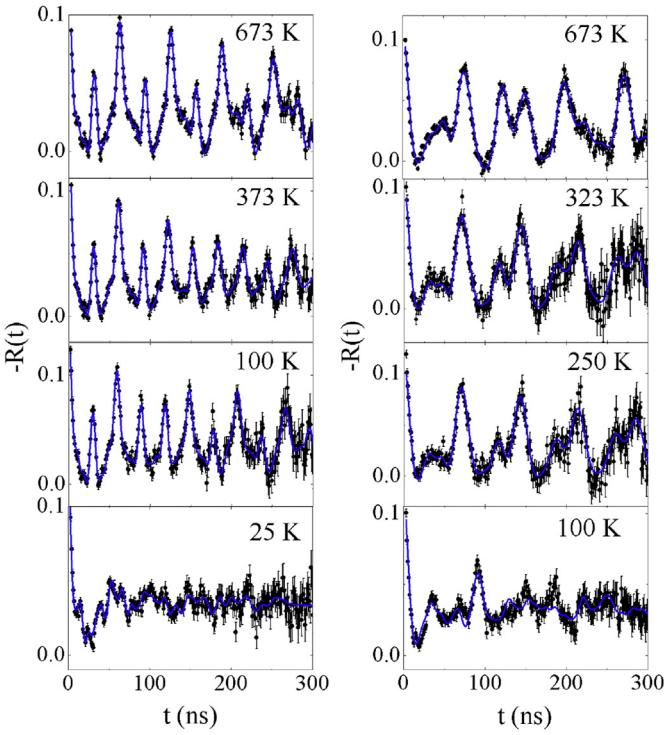

Fig. 3. Representative curves of PAC spectra measured above and below the magnetic transition of (left) $Bi_2Mn_4O_{10}$ (T_N = 39 K) and (right) $Bi_2Fe_4O_9$ (T_N = 250 K). The solid lines represent the theoretical fitting (pure electric quadrupole interactions above T_N and combined electric quadrupole plus magnetic dipole interactions below T_N).

In order to interpret the PAC hyperfine parameters, it is first necessary to determine the localization of the probe nuclei ^{111}In (^{111}Cd) into the crystalline structure. In the sample $Bi_2Mn_4O_{10}$ ($Bi_2Fe_4O_9$), there are three crystallographic sites which can be occupied by the probe nuclei – the Mn^{4+} (Fe^{3+}) octahedral site, the Mn^{3+} pyramidal (Fe^{3+} tetrahedral) site, and the polyhedral site Bi^{+3}. In this context, we have taken into account four considerations: (i) the charge affinity which indicates that the probe nuclei can preferentially substitute ions with the same valence Mn^{+3}, Fe^{3+}, and Bi^{+3}; (ii) several works have shown that in other transition metal oxides, ^{111}In tend to preferentially occupy the octahedral sites [21]; (iii) for perovskites compounds ABO_3, PAC measurements

Table 1
Experimental and calculated DFT hyperfine parameters (EFG and asymmetry) for pure and Cd impurity in several sites for $Bi_2Mn_4O_{10}$ and $Bi_2Fe_4O_9$ samples. Fe1: octahedral site and Fe2: tetrahedral site.

$Bi_2Mn_4O_{10}$(Cd) (calculated)			$Bi_2Mn_4O_{10}$(Cd) (experimental)		
Site	EFG ($\times 10^{21}$ V/m)	η	EFG	η	f(%)
Cd(Bi)	−6.87	0.51			
Cd(Mn^{4+})	−3.54	0.49	3.56	0.7	45
Cd(Mn^{3+})	11.6	0.24	12.1	0.01	55
$Bi_2Fe_4O_9$(Cd) (calculated)			$Bi_2Fe_4O_9$(Cd) (experimental)		
Site	EFG ($\times 10^{21}$ V/m)	η	EFG	η	f(%)
Cd(Bi)	−12.1	0.374			
Cd(Fe1)	−5.23	0.431	4.97	0.2	80
Cd(Fe2)	4.98	0.91	6.43	0.7	20

have revealed that the probe nuclei localized in polyhedral (octahedral B) sites A exhibit a higher (smaller) quadrupolar frequencies and smaller (higher) asymmetry parameter [22–25]; (iv) first principles calculations based on density functional theory were performed for the two samples studied. These calculations were obtained by considering the localization of probe nuclei Cd in the three crystallographic sites present in each sample. The theoretical and experimental values of the electric field gradient and the asymmetry parameter obtained for each sample are showed in Table 1.

Taking into account the rules outlined above, the hyperfine parameters determined experimentally could be clearly assigned to each crystallographic site occupied by the probes. Comparing the experimental and theoretical values of the EFG and asymmetry parameters, one can conclude that ^{111}In (^{111}Cd) nuclear probes do not occupy Bi sites in both compounds. The calculated values of hyperfine parameters agree well with the experimental ones for $Bi_2Mn_4O_{10}$. For $Bi_2Fe_4O_9$, the experimental value of the EFG for the Fe1 site is close to the calculated value of Fe2 site while the asymmetry parameters tendency compares well between experiment and theory. The reason for this discrepancy is that the difference between the two EFG is not large and calculations involving larger super-cells are needed in order to increase precision. On the other hand, the high quadrupole frequency (large EFG) with low asymmetry parameter at room temperature observed for $Bi_2Mn_4O_{10}$, can be ascribed to ^{111}Cd probe nuclei at pyramidal position of Mn^{3+}. The preference of this pyramidal site occupation comes from the charge affinity between the probe nuclei and Mn^{+3} ions. This is reinforced by our calculations where the results show that the high EFG with low asymmetry parameters correspond to the pyramidal sites. The octahedral Mn^{3+} sites present a smaller EFG and large asymmetry parameter as usually found in perovskites. Also, the calculated value agrees very well with this assignment. For the sample $Bi_2Mn_4O_{10}$, it is observed the value of f is very similar for octahedral and pyramidal sites. This result suggests that the probe nuclei are homogeneously distributed in both sites. However, for the sample $Bi_2Fe_4O_9$ the major value of f corresponds to parent nuclei ^{111}Cd localized in octahedral sites which may be due to the charge affinity and to the preference of probe nuclei by octahedral sites.

Fig. 4(a) and (b) show the Fourier transform of the PAC spectra measured at 673 K for both $Bi_2Mn_4O_{10}$ and $Bi_2Fe_4O_9$ compounds. We can clearly observe two set of frequencies due to quadrupole interactions on ^{111}Cd occupying octahedral and pyramidal sites in $Bi_2Mn_4O_{10}$. The pyramidal site of $Bi_2Mn_4O_{10}$ exhibits three well-defined peaks, corresponding to a single EFG. However, the octahedral site of $Bi_2Mn_4O_{10}$ displays only two well-defined peaks at $T = 673$ K, this effect is due the overlap of the two first peaks. This overlap is due to an increase of the asymmetry parameter that reaches values around of η ~1. These peaks exhibit a small broadening of the frequency at both sites suggesting the presence of probe nuclei at cationic positions which are relatively free from defects. On the other hand, the octahedral site of $Bi_2Fe_4O_9$ shows also three well-defined peaks at $T = 673$ K corresponding to a

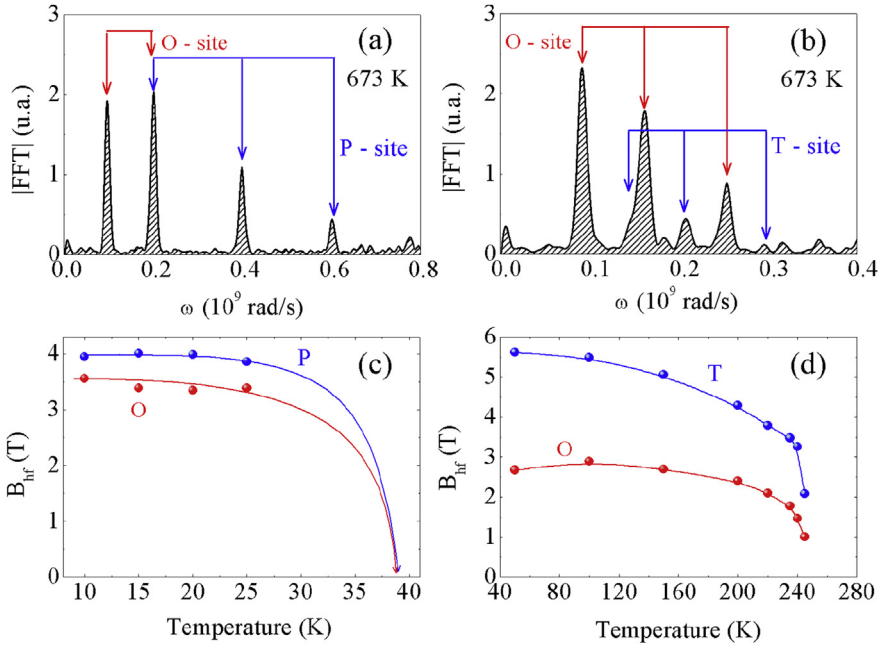

Fig. 4. Fast Fourier transforms (FFT) of PAC spectra measured at $T = 673$ K for (a) $Bi_2Mn_4O_{10}$ and (b) $Bi_2Fe_4O_9$. Temperature dependence of hyperfine magnetic field for (c) $Bi_2Mn_4O_9$ and (d) $Bi_2Fe_4O_9$. O: octahedral, P: pyramidal, and T: tetrahedral. Blue and red lines are guides for the eyes. (For interpretation of the references to color in this figure legend, the reader is referred to the web version of this article.)

quadrupole interaction with small asymmetry parameter η and with population of 80%. Note that the tetrahedral site of $Bi_2Fe_4O_9$ exhibits three very broad peaks and with low intensity. The relatively large width of these peaks suggests a high frequency distribution revealing a considerable dispersion in the value of η of the tetrahedral sites. Fig. 4(c) and (d) shows the temperature dependence of the hyperfine magnetic field obtained from the fitting for $Bi_2Mn_4O_{10}$ and $Bi_2Fe_4O_9$, respectively. In both samples, it is observed that the macroscopic antiferromagnetic transition is accompanied by the appearance of a hyperfine magnetic field. The presence of the hyperfine magnetic field is observed in all crystallographic sites – octahedral, pyramidal, and tetrahedral. B_{hf} is smaller for probe nuclei localized at the octahedral sites of both compounds than those localized at tetrahedral or pyramidal sites. This difference is due to the fact that each crystallographic site has a different number of nearest neighbor ions. In $Bi_2Mn_4O_{10}$ the superexchange interaction is responsible by the magnetic coupling between Mn ions so that the Mn^{4+}–O–Mn^{3+}–O–Mn^{4+} indirect interaction is dominant resulting in a ferromagnetic coupling of Mn^{4+} neighbors separated by Mn^{3+} planes [12]. In this scenario, when ^{111}Cd probes are at tetrahedral Mn^{3+} sites their neighbors are ferromagnetically coupled Mn^{4+} cations, which results in a higher B_{hf} than that when ^{111}Cd probes are at octahedral Mn^{4+} sites with Mn^{3+} neighbors. A similar situation is found in $Bi_2Fe_4O_9$, however um higher B_{hf} for ^{111}Cd at tetrahedral sites. The values of B_{hf} also confirm the correct site assignment of the nuclear probes.

3.3. Local evidence of magneto-electric coupling

It is well known that the electric field gradient and magnetic hyperfine fields are very sensitive to the local symmetry where the nuclear probes are located. Therefore, evidence about the possible coupling between the magnetic and electrical properties of our samples can be obtained by studying the temperature evolution of the hyperfine parameters (B_{hf}, ν_Q and η). The study of the local magnetic hyperfine field provides information on how the macroscopic antiferromagnetic ordering affects the local structure of the spins in each crystallographic site along with charge polarization. Fig. 5 shows the temperature dependence of the quadrupolar frequency and asymmetry parameter. In both samples, it is observed that the quadrupolar frequency initially displays a slightly linear increasing behavior by decreasing the temperature for all crystallographic sites. However, ν_Q undergoes an anomalous variation close to $T_N = 39$ K for $Bi_2Mn_4O_{10}$. For $Bi_2Fe_4O_9$ sample, this anomalous variation is observed only for tetrahedral site at 250 K. The antiferromagnetic phase transition at $T_N = 39$ K and 250 K also induces anomalous variation in the asymmetry parameter of pyramidal site (tetrahedral) for $Bi_2Mn_4O_{10}$ ($Bi_2Fe_4O_9$) compounds. One can see that the asymmetry parameter of the octahedral site of both samples decreases slightly by decreasing the temperature. Note that η also exhibits an anomalous change close to magnetic transition temperature.

Anomalous local behavior of the EFG tensor and asymmetry parameter (η) around magnetic transition in other multiferroic compounds such as $Pr_{1-x}Ca_xMnO_3$ and $AgCrO_2$ were reported in the literature [26,27]. In these works, it was suggested that the temperature dependence of EFG tensors can give information on the onset of charge or orbital ordering and support the idea that distortion of oxygen coordination emerging below transition temperature could be correlated with short-range magnetic interactions. Correlations of magneto-elastic instability can be a channel for magnetic frustration. Therefore, the magneto-electric coupling is related to the geometrically frustrated magnetic structure that both compounds $Bi_2Fe_4O_9$ and $Bi_2Mn_4O_{10}$ exhibit. Such as magneto-elastic frustration is released below the antiferromagnetic ordering. This decrease in frustration is driven by spontaneous magnetostriction effect – displacement of Mn/Fe ions which modifies its equilibrium positions inducing distortions of oxygen coordination as reveled in Fig. 5 for both systems. Indeed, in mixed valence (Mn^{3+} and Mn^{4+}) $Bi_2Mn_4O_{10}$, a charge ordering reorientation along the *b* axis takes place below the Neel temperature. The combined action of these two effects breaks the inversion symmetry of the system leading to the onset of macroscopic electrical polarization. On the other hand, the displacement of Fe ions in $Bi_2Fe_4O_9$ is sufficient to break the inversion symmetry generating also an electrical polarization. Note that the alteration of the equilibrium positions of the Mn/Fe ions may modifies the local electronic surroundings of the nuclear probes changing hyperfine parameters. The anomalous behavior of the quadrupolar frequency and the asymmetry parameter observed close to magnetic transition temperature suggests a strong coupling between magnetic, electric, and elastic properties below the Neel temperature of both samples.

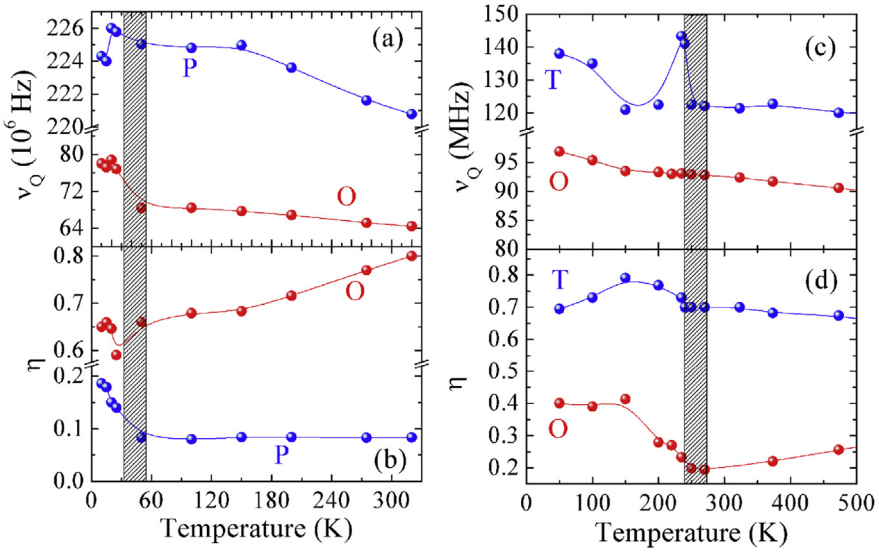

Fig. 5. Temperature dependence of the quadrupolar coupling frequency (ν_Q) and asymmetry parameter (η) obtained at low temperatures for (a–b) $Bi_2Mn_2O_{10}$ and (c–d) $Bi_2Fe_4O_9$. O: octahedral, P: pyramidal, and T: tetrahedral. Lines are guide to the eye.

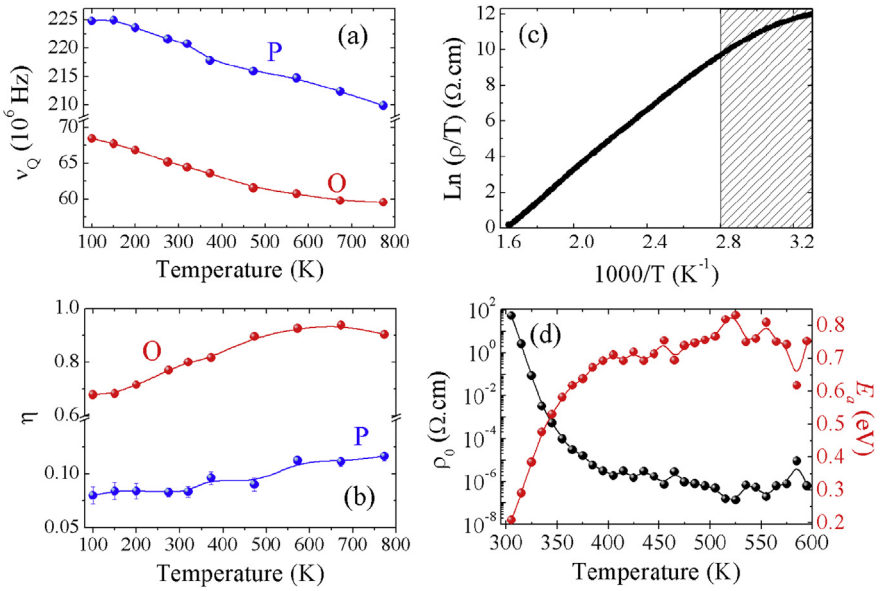

Fig. 6. Temperature dependence of (a) quadrupolar frequency (ν_Q) and (b) asymmetry parameter (η). (c) Electrical resistivity plotted in the adiabatic regime of the small polaron model. (d) The prefactor ρ_0 and activation energy E_a as a function of temperature for $Bi_2Mn_4O_{10}$. O: octahedral, P: pyramidal, and T: tetrahedral. Lines are guides for the eyes.

3.4. Correlation between electric transport properties and local distortions

The change in the equilibrium positions of the atoms according to octahedral, tetrahedral and pyramidal environments, which will affect the local environment of the nuclear probes, has been monitored by the temperature dependence of hyperfine parameters. Fig. 6(a) and (b) show the temperature evolution of the quadrupolar frequency and asymmetry parameter for $Bi_2Mn_4O_{10}$ sample. One can observe that the quadrupole frequency (asymmetry parameter) of the pyramidal site is much larger (smaller) than that of the octahedral site. Note that the values of η for the pyramidal site are small, being its maximum value around 0.12, indicating a high degree of symmetry of this crystallographic site. By increasing the temperature, we have observed three effects: (i) the quadrupole frequency (ν_Q) in both crystallographic sites linearly decreases; (ii) the value of η for the octahedral site increases; (iii) the value of η for pyramidal site displays a nearly constant behavior in the entire studied temperature range.

The electric transport mechanism of both samples was studied by using the adiabatic regime of the small polaron hopping model. In this regime, the electrical resistivity is described by the equation $\rho = \rho_0 T \exp(E_a/k_B T)$, where ρ_0 is a pre-factor, which is inversely proportional to the hopping frequency (Ω_0) of the charge carries and E_a is the activation energy. Note that from this equation, it is expected a linear behavior of the curve Ln(ρ) vs T^{-1} which is plotted in Fig. 6(c). However, it is observed a pronounced curvature instead of linearity over the entire studied temperature range. Note that the curvature is more pronounced from room temperature up to ~380 K. A similar behavior was found by using the non-adiabatic regime of the small polaron model and the Arrhenius equation. This result suggests that the pre-factor ρ_0 and activation energy are dependent on temperature. In this context, we have estimated the evolution with temperature of ρ_0 and E_a by performing a linear fitting in small temperature intervals ($\Delta T = 10$ K) using the adiabatic regime of the small polaron model. The results are showed in Fig. 6(d). For the temperature range 300 K < T < 400 K, we have observed a strong decrease (increase in E_a) of ρ_0. Note that the decrease in ρ_0 indicates an increase of hopping frequency Ω_0. The evolution of E_a and Ω_0 has different effects on the electrical resistivity value. The increase of E_a leads to reduction of the electrical conductivity whereas the increase of Ω_0 rises the electrical conductivity of the system. Above 420 K, an almost constant behavior is observed in both parameters.

In the small polaron model, the polaron quasiparticle is formed by the interaction between charge carriers and ions in the lattice conforming the molecular crystal. If this interaction is strong enough it will induce a change in the equilibrium positions of these ions producing a potential well where the charge carriers become localized. In this model, the activation energy is proportional to the interaction energy between the charge carriers and crystal molecules and to the polaron binding energy. The interaction energy (charge carriers and molecules) is also proportional to the distortion degree of crystal structure. The hopping frequency is defined as $\Omega_0 = (J^4\pi/4\hbar^2 E_a k_B T)^{1/2}$, where J is the exchange interaction constant between nearest neighbors. The value of J depends strongly on the distance of these nearest neighbors and, consequently, it can be modified by local distortions. Therefore, changes in the equilibrium positions of the ions conforming the octahedral, tetrahedral and pyramidal ions of our samples, can modify the activation energy and hopping frequency of the system. In this context, we believe that the temperature dependence of ρ_0 and E_a is caused by two effects (i) the electronic hopping between nonequivalent crystallographic sites with different local symmetry (octahedral and pyramidal sites) and (ii) the modification of the local octahedral structure (increase of η) caused by anharmonic thermal effect.

Fig. 6 shows instabilities at high temperature: slight alteration in the slope of the linear behavior of η and ν_Q; E_a and ρ_0 exhibit change in curvature above ~425 K. It has been reported that the compound $Bi_2Mn_4O_{10}$ exhibits anomalous behavior in the frequency dependence of the dielectric constant at high temperatures [28,29]. This behavior has been attributed to the existence of polar nanoregions whose formation mechanism is not fully understood yet. These nanoregions would form ferroelectric islands embedded in a paraelectric matrix [30]. Fier *et. al* [31]. showed that the relaxation frequency of this compound obeys the Vogel-Fulcher equation at intermediate range temperature which is a behavior expected for ferroelectric relaxations. Since in this temperature range there is no

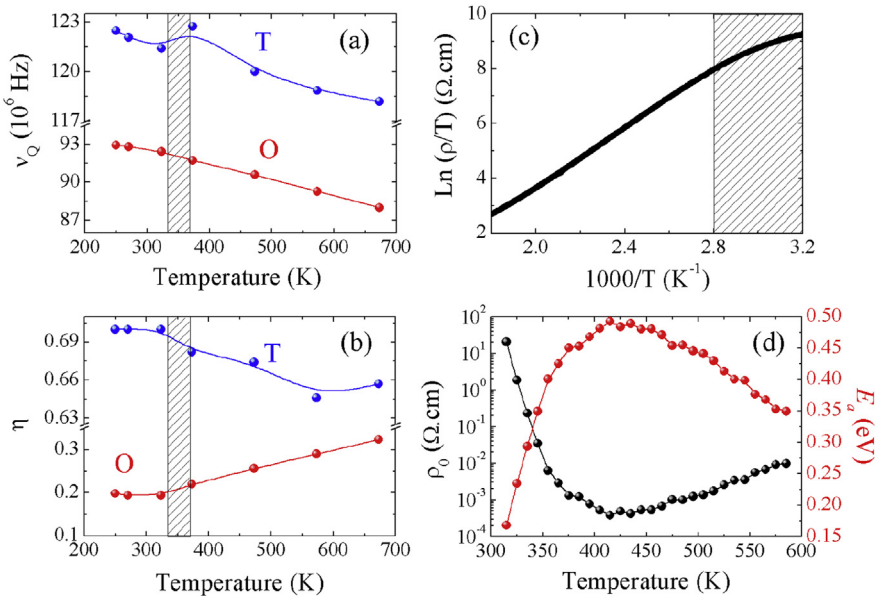

Fig. 7. Temperature dependence of the (a) quadrupolar frequency and (b) asymmetry parameter obtained at high temperatures. (c) Electrical resistivity plotted in the adiabatic regime of the small polaron model. (d) The prefactor ρ_0 and activation energy E_a as a function of temperature for $Bi_2Fe_4O_9$. O: octahedral, P: pyramidal, and T: tetrahedral. Lines are guides for the eyes.

long-range magnetic order, a possible origin could be associated with the distortion of the polyhedron BiO_8 [31] breaking the space inversion symmetry of the system, leading to electrical polarization within nanoregions. We believe that the displacement of Bi^{3+} can modify the local environment of the probe nuclei, causing the anomalous instabilities in hyperfine parameters, but it is very subtle as observed in Fig. 6(a) and (b).

A similar analysis has been done for $Bi_2Fe_4O_9$ compound. From Fig. 7(a) and (b), one can see that in the entire measured temperature range, the values of ν_Q and η for the tetrahedral site are larger than those for the octahedral site. This behavior indicates that the tetrahedral local structure is more distorted and has a higher local electric field gradient. By increasing the temperature, it is observed three effects: (i) the quadrupolar frequency for the tetrahedral site decreases with the temperature. Note also that close to 360 K, the quadrupole frequency of this crystallographic site exhibits an anomalous behavior (sudden increasing). Above this temperature, ν_Q also decreases but with different slope. (ii) The quadrupolar frequency for octahedral site decreases monotonically with the temperature and (iii) below 360 K, the behavior of the asymmetry parameter is temperature independent for the two crystallographic sites. However, above this temperature, the value of η for octahedral site (tetrahedral) increases (decreases) monotonically with the temperature. Fig. 7(c) shows the electrical resistivity of $Bi_2Mn_4O_{10}$ plotted in the form Ln(ρ) vs T^{-1}. From this figure, we have also observed a pronounced curvature suggesting ρ_0 and E_a are not constants in this compound as well. The values of ρ_0 and E_a as a function of temperature ($\Delta T = 10$ K) are showed in Fig. 7(d). In this case, the temperature dependence of E_a and ρ_0 is caused by electronic hopping between nonequivalent crystallographic sites (octahedral and tetrahedral sites) and alteration of the local crystalline structure due to thermal energy. Our results suggest that anharmonic effects are much more pronounced in the temperature range between 300 and 360 K.

4. Conclusions

We have performed a local and macroscopic study on the magnetic and electrical properties of $Bi_2Mn_4O_9$ and $Bi_2Fe_4O_9$ compounds. The long range antiferromagnetic ordering is accompanied by an anomalous behavior of the quadrupolar frequency (electrical field gradient) and asymmetry parameter in both samples. This anomalous behavior was explained as due to displacement of Mn/Fe ions from its equilibrium position caused by the magnetostriction effect. This effect is responsible by the onset of macroscopic electrical polarization in both compounds. We believe that these results reveal the correlations between magnetic, electric, and elastic interactions. We have found that the hopping frequency and activation energy are temperature dependent which are closely related to hyperfine parameters. The analysis of both ν_Q and η at high temperatures revealed that the charge carrier transport behavior is caused by modifications in the equilibrium positions of oxygen atoms forming octahedral, pyramidal and tetrahedral environments.

Acknowledgments

This material is based upon work supported by the Brazilian agency CNPq under grants No. 485405/2011-3, 305772/2011-2, and 455092/2014-1 and Fapesp under grant No. 2013/16172-5.

References

[1] M.M. Kumar, V.R. Palkar, K. Srinivas, S.V. Suryanarayana, Appl. Phys. Lett. 76 (2000) 2764.
[2] T. Kimura, S. Kawamoto, I. Yamada, M. Azuma, M. Takano, Y. Tokura, Phys. Rev. B 67 (2003) 180401.
[3] Z.H. Chi, C.J. Xiao, S.M. Feng, F.Y. Li, C.Q. Jin, X.H. Wang, R.Z. Chen, L.T. Li, J. Appl. Phys. 98 (2005) 103519.
[4] G. Catalan, J.F. Scott, Adv. Mater. 21 (2009) 2463.
[5] W. Eerenstein, N.D. Mathur, J.F. Scott, Nature 442 (2006) 759.
[6] H. Zhang, M. Richter, K. Koepernik, I. Opahle, F. Tasndi, H. Eschrig, New J. Phys. 11 (2009) 43007.
[7] C.N.R. Rao, R.J. Serrao, J. Mater. Chem. 17 (2007) 4931.
[8] S.W. Cheong, M. Mostovoy, Nat. Mater. 6 (2007) 13.
[9] A. Sing, V. Pandey, R.K. Kotnala, D. Pandey, Phys. Rev. Lett. 101 (2008) 247602.
[10] N. Niizaki, M. Wachi, Z. Kristaogr. Krist. Krist. Kristalchem. 127 (1968) 173.
[11] H. Schneider, J. Schreuer, B. Hildmann, J. Eur. Ceram. Soc. 28 (2008) 239.
[12] A. Muñoz, J.A. Alonso, M.T. Casais, M.J. Martínez-Lope, J.L. Martínez, M.T.F. Díaz, Phys. Rev. B 65 (2002) 144423.

[13] E. Ressouche, V. Simonet, B. Canals, M. Gospodinov, V. Skumryev, Phys. Rev. Lett. 103 (2009) 267204.
[14] A.P. Ramirez, Annu. Rev. Mater. Sci. 24 (1994) 453.
[15] J.V. Brink, D.I. Khomskii, J. Phys. Condens. Matter 20 (2008) 434217.
[16] R.A. Brand, NORMOS Mössbauer Fitting Program, 1995.
[17] P. Blaha, K. Schwarz, G.K.H. Madsen, D. Kvasnicka, J. Luitz, WIEN2k, an Augmented Plane Wave + Local Orbitals Program for Calculating Crystal Properties, Karlheinz Schwarz, Techn. Universität Wien, Austria, 2001.
[18] J.P. Perdew, S. Burke, M. Ernzerhof, Phys. Rev. Lett. 77 (1996) 3865.
[19] P.E. Blöchl, O. Jepsen, O.K. Andersen, Phys. Rev. B 49 (1994) 16223.
[20] Z.R. Kann, J.T. Auletta, E.W. Hearn, S. U.Weber, K.D. Becker, H. Schneider, M.W. Lufaso, J. Sol. State Chem. 185 (2012) 62.
[21] D. Lupascu, Nucl. Instrum. Methods B 113 (1996) 507.
[22] R. Dogra, A.C. Junqueira, R.N. Saxena, A.W. Carbonari, J. Mestnik-Filho, M. Morales, Phys. Rev. B 63 (2001) 224104.
[23] H. Haas, J.G. Correia, Hyperfine Interact. 198 (2010) 13.
[24] J.N. Gonçalves, A. Stroppa, J.G. Correia, T. Butz, S. Picozzi, A.S. Fenta, V.S. Amaral, Phys. Rev. B 86 (2012) 035145.
[25] T.M. Rearick, G.L. Catchen, J.M. Adams, Phys. Rev. B 48 (1993) 224.
[26] A.M.L. Lopes, G.N.P. Oliveira, T.M. Mendonça, J. Agostinho Moreira, A. Almeida, J.P. Araujo, V.S. Amaral, J.G. Correia, Phys. Rev. B 84 (2011) 014434.
[27] A.M.L. Lopes, J.P. Araujo, V.S. Amaral, J.G. Correia, Y. Tomioka, Y. Tokura, Phys. Rev. Lett. 100 (2008) 155702.
[28] A.A. Bokov, Z.-G. Ye, J. Mater. Sci. 41 (2006) 31.
[29] F. HuiQing, K.E. ShanMin, Sci. China Ser. E Technol. Sci. 52 (2009) 2180.
[30] G. Burns, F. Dacol, Phys. Rev. B 28 (1983) 2527.
[31] I. Fier, L. Walmsley, J.A. Souza, J. Appl. Phys. 110 (2011) 084101.